

Supporting Information

Oxygen defect engineering on low-crystalline iron(III) oxyhydroxide as highly efficient electrocatalyst for water oxidation

Yaning Fan^a, Junjun Zhang^{a*}, Kongliang Luo^a, Xuanyu Zhou^a, Jiahua Zhao^b, Weiwei Bao^c, Hui Su^d, Nailiang Wang^{a*}, Pengfei Zhang^{a,b}, Zhenghong Luo^{a, b}

[a]State Key Laboratory of High-Efficiency Utilization of Coal and Green Chemical Engineering. College of Chemistry and Chemical Engineering, Ningxia University, Yinchuan, Ningxia, 750021, China.

[b]School of Chemistry and Chemical Engineering, Shanghai Jiao Tong University, Shanghai, 200240, P. R. China

[c]National & Local Joint Engineering Laboratory for Slag Comprehensive Utilization and Environmental Technology, School of Material Science and Engineering, Shaanxi University of Technology, Hanzhong, Shaanxi, 723000 P. R. China

[d]Department of Chemistry, FRQNT Centre for Green Chemistry and Catalysis, McGill University, 801 Sherbrooke Street W., Montreal, QC H3A 0B8, Canada

*Corresponding authors

Email address:

zhangjj089@nxu.edu.cn (J.J. Zhang); wangnl@nxu.edu.cn (N. L. Wang);

List of Contents

1 Experiment Section

1.1 Materials

1.2 Preparation of FeOOH

1.3 Electrode preparation

1.4 Electrochemical characterizations

1.5 Material characterizations

1.6 Computational details

2. Supplementary Figures:

Fig. S1 Representation of catalyst preparation process.

Fig. S2 a) V_O-FeOOH powder and b) FeOOH powder sample.

Fig. S3 V_O-FeOOH, FeOOH, and IrO₂ ink-loaded electrodes and Ni foam (From left to right).

Fig. S4 XPS survey scan of V_O-FeOOH sample.

Fig. S5 Barrett-Joyner-Halenda(BJH) pore size distribution for V_O-FeOOH sample.

Fig. S6 AFM image of V_O-FeOOH sample.

Fig. S7 The EDS of V_O-FeOOH sample.

Fig. S8 SAED pattern of V_O-FeOOH sample.

Fig. S9 Electrochemical properties of V_O-FeOOH with different loadings (25, 50, 75, 100, 125 μ L). a) LSV curves, b) EIS, c) Tafel slopes, d) overpotentials based 50 and 100 mA cm⁻².

Fig. S10 CV curves of electrodes at different scan rates from 20 to 100 mV s⁻¹. a) V_O-FeOOH, b) IrO₂, c) NF.

Fig.S11 The electrochemical impedance spectroscopy equivalent circuit diagram.

Fig. S12 The Operando Nyquist of a) IrO₂ and b) NF at various overpotentials in 1.0 M KOH electrolyte. (Inset in Fig. S3b: partially enlarged image).

Fig. S13 The Bode phase plots of a) IrO₂ and b) NF at various overpotential in 1.0 M KOH electrolyte.

Fig.S14 a) In-situ Nyquist and b) Bode phase diagrams of V_O-FeOOH samples supported on carbon cloth at different overpotentials in 1.0 M KOH electrolyte.

Fig.S15 The long-time E-t curves of V_O-FeOOH for OER under a constant current of 100 mA cm⁻².

Fig.S16 a) The two-electrode water splitting device diagram, b) amplification schematic diagram of two-electrode water splitting device, c) LSV plots of the V_O-FeOOH||Pt/C, RuO₂||Pt/C for overall alkaline water splitting, d) E-t curve of V_O-

FeOOH||Pt/C for overall water splitting at 10 mA cm⁻² in 1.0 M KOH electrolyte.

Fig.S17 a) SEM image of V_O-FeOOH NF before OER and b) SEM image, c) TEM image, b) HRTEM image, c) the different regions corresponding intensity profiles along with the position of V_O-FeOOH after OER.

Fig. S18 XRD patterns of FeOOH and standard card.

Fig.S19 The a) HR-TEM image and b) the different regions corresponding intensity profiles along with the position of FeOOH.

Fig. S20 The XPS spectrum of FeOOH sample.

Fig.S21 O1s high resolution XPS spectra of V_O-FeOOH and FeOOH samples.

Fig. S22 Fe2p high resolution XPS spectra of V_O-FeOOH and FeOOH samples.

Fig. S23 Comparison of overpotential of V_O-FeOOH and FeOOH samples at different current density.

Fig. S24 a) CV curves of electrodes at different scan rates from 20 to 100 mV s⁻¹ of FeOOH, b) The C_{dl} obtained at the specific potential of synthesized V_O-FeOOH and FeOOH samples.

Fig. S25 a) N₂ adsorption-desorption isotherms and b) Barrett-Joyner-Halenda(BJH) pore size distribution for FeOOH sample.

Fig. S26 Density of states of (a) V_O-FeOOH and (b) FeOOH samples, respectively.

Fig. S27 Optimized configurations of a) V_O-FeOOH and b) O*, c) OH*, and d) OOH* species adsorbed on V_O-FeOOH sample.

Fig. S28 Optimized configurations of a) FeOOH and b) O*,c) OH*,and d) OOH* species adsorbed on FeOOH samples.

3. Supplementary Tables

Table S1. Comparison of the OER performance of V_O-FeOOH catalyst with other reported OER catalysts

4.Reference

1. Experiment Section

1.1 Materials

NaBH₄ (Sinopharm Chemical Reagent Co., Ltd. analytically pure), Fe(NO₃)₃·9H₂O (Aladdin, ≥ 99.9%), IrO₂ (Macklin, Ir ≥ 84.5%), FeCl₃ (Macklin, analytically pure), NaNO₃ (Sinopharm Chemical Reagent Co., Ltd. analytically pure), Nafion dispersion, anhydrous ethanol (99.9%), hydrochloric acid (37%), acetone, deionized water. All chemicals were used as received without further purification.

1.2 Preparation of FeOOH

5mmol FeCl₃ and 20mmol NaNO₃ were dissolved in 50ml deionized water, ultrasonic until completely dissolve¹⁻². After stirring and heating to 100°C, it was kept for 15min. The cooled reaction liquid was centrifuged, rinsed and dried. The brick red powder (Fig. S2b), denoted as FeOOH, was obtained.

1.3 Electrode preparation

Nickel foam was cut into small rectangular pieces of 1*3cm². After ultrasonic cleaning with 3mol L⁻¹ HCl for 15 min, they were washed with deionized water, anhydrous ethanol and acetone for three times. After absorbing the surface moisture, they were placed in a vacuum drying oven at 60°C for 6h.

5.0 mg V_O-FeOOH, FeOOH and IrO₂ were added into a 1.5ml centrifuge tube, and 600uL deionized water, 400uL dehydrated alcohol and 10uL nafion dispersion were added with a pipette gun, and ultrasounded for 60 min. The prepared ink was applied to NF (1*1cm²) with a pipette at 25 uL each time, and dried for 15 min after each application, for a total of 4 times (Fig. S2). In order to seek the best performance, five samples of 25, 50, 75, 100 and 125 uL were prepared, which were recorded as V_O-FeOOH₂₅(25uL), V_O-FeOOH₅₀(50uL), V_O-FeOOH₇₅(75uL), V_O-FeOOH₁₀₀(100uL) and V_O-FeOOH₁₂₅(125uL). The electrochemical performance test shows that V_O-FeOOH₁₀₀ has the best chemical performance, denoted as V_O-FeOOH.

1.4 Electrochemical characterizations

Electrochemical performance tests were performed at room temperature using an electrochemical workstation (DH7000C, Donghua, Jiangsu, China). V_O-FeOOH,

FeOOH and IrO₂ were uniformly coated on nickel foam as working electrode, graphite rod and standard Hg/HgO electrode as counter electrode and reference electrode, 1 M KOH as electrolyte. At the beginning of the experiment, the catalyst was subjected to 20 cycles of cyclic voltammetry (CV) at 10mV/s at 0.5-1.2V to stabilize the catalyst surface. The oxygen evolution performance of the catalyst was determined by linear sweep voltammetry (LSV) in the range of 0-1.2V vs. Hg/HgO. Double layer capacitance (C_{dl}) measurements were conducted by varying the scan rates (20, 40, 60, 80, 100mV/s) in a potential window nearly without Faradaic process. The electrochemical impedance spectroscopy (EIS) test was performed in the frequency range of 0.1-1000Hz, and the in-situ impedance of the catalyst was measured using EIS in the range of 0.45-0.80V. The turnover frequency (TOF) of the electrode was calculated at 1.55 V and 1.60 V. In the range of 0.5-1.2 V, 500 CV cycles were carried out at a scan rate of 50 mV s⁻¹. The stability of the catalyst was evaluated by comparing the LVS and EIS before and after 500 CV cycles. The long-term stability of the catalyst was tested at 50 mA cm⁻². At the same time, multi-steps current 10, 30, 50, 70, 90, 110 mA cm⁻² and multi-steps potential 1.524, 1.574, 1.624, 1.674, 1.724 V vs.RHE were used to evaluate the stability of the catalyst in the dynamic current and dynamic potential. The conversion formula between the measured value and the standard hydrogen electrode (RHE) is:

$$E_{RHE} = E_{Hg/HgO} + 0.059pH + 0.098V$$

The calculation formula of overpotential η :

$$\eta = E_{RHE} - 1.23V$$

Tafel slope calculation formula :

$$\eta = b \log j + a$$

The formula for calculating the turnover frequency (TOF) :

$$TOF = \frac{jA}{4nF}$$

1.5 Material characterizations

The X-ray diffraction (XRD) patterns were recorded on a Rigaku MiniFlex 600-C

X-ray diffractometer with Cu-K α radiation with a scan rate of 5° min⁻¹. The electron paramagnetic resonance (EPR) spectra were collected on a Bruker A300 Paramagnetic spectrometer, which were performed at room temperature in vacuum. The thickness of the nanosheets was measured by atomic force microscopy (AFM). The Raman measurement was performed with a Raman JY HR800 Spectrometer, wavenumber region 150-600 cm⁻¹. The Brunauer Emmett Teller (BET) pore size distribution method using a Micromeritics ASAP 2460. The Scanning electron microscopy (SEM) characterizations were conducted using a JSM-7800F from JEOL. Transmission electron microscopy (TEM) and high-resolution transmission electron microscopy (HRTEM) measurements were taken with a JEOL JEM-F200 microscope operated. The X-ray photoelectron spectroscopy (XPS) measurements were conducted on a Kratos Axis Ultra DLD spectrometer.

1.6 Computational details

All the density functional theory calculations were performed by using the Vienna ab initio Simulation Program (VASP)³. The generalized gradient approximation (GGA) in the Perdew-Burke-Ernzerhof (PBE) form and a cutoff energy of 500 eV for planewave basis set were adopted⁴⁻⁶. A 3 \times 3 \times 1 Monkhorst-Pack grid was used for sampling the Brillouin zones at structure optimization⁷. The ion-electron interactions were described by the projector augmented wave (PAW) method⁸. The convergence criteria of structure optimization were choose as the maximum force on each atom less than 0.02 eV/Å with an energy change less than 1 \times 10⁻⁵ eV. The DFT-D3 semiempirical correction was described via Grimme's scheme method⁹. The Gibbs free energy change (ΔG) for each elemental step is defined as¹⁰:

$$\Delta G = \Delta E + \Delta ZPE - T\Delta S + \Delta G_U + \Delta G_{\text{pH}} \quad (1)$$

where ΔE and ΔZPE are the adsorption energy based on density functional theory calculations and the zero-point energy correction, respectively. T , ΔS , U , and ΔG_{pH} represent the temperature, the entropy change, the applied electrode potential, and the free energy correction of the pH, respectively. In alkaline medium, the reaction mechanism of OER is mainly AEM mechanism. The oxygen precursor undergoes a

process of adsorption-deprotonation-coupling-desorption. The metal sites first adsorb OH-, and then deprotonate to form *O species. The O-O coupling generates *OOH intermediates through OH-nucleophilic attack. Finally, the surface desorbs O₂ molecules through secondary deprotonation to release active metal sites. According to the above theory, we believe that Fe ions are active centers in V_O-FeOOH catalyst, so the reaction energy required for the formation of active intermediates was calculated by AEM in the present situation.

2. Supplementary Figures:

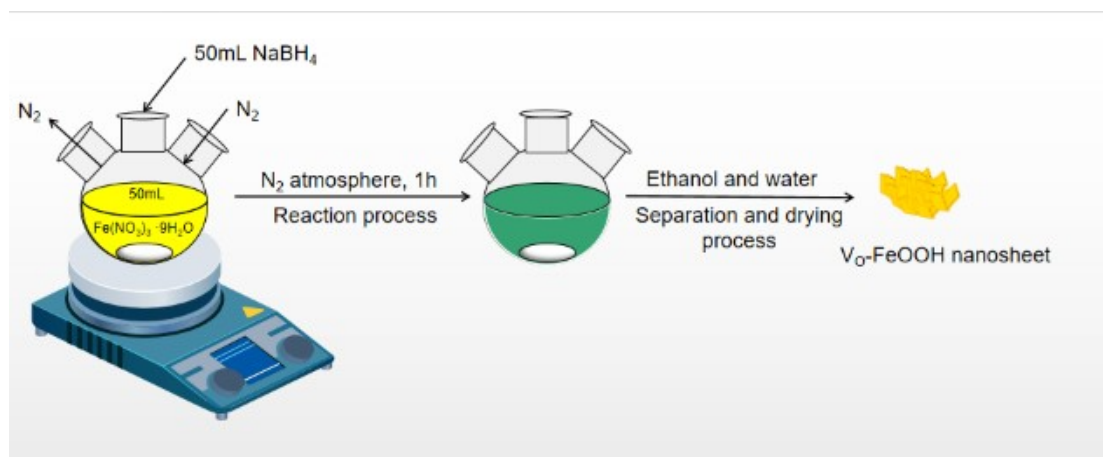


Fig. S1 Representation of catalyst preparation process.

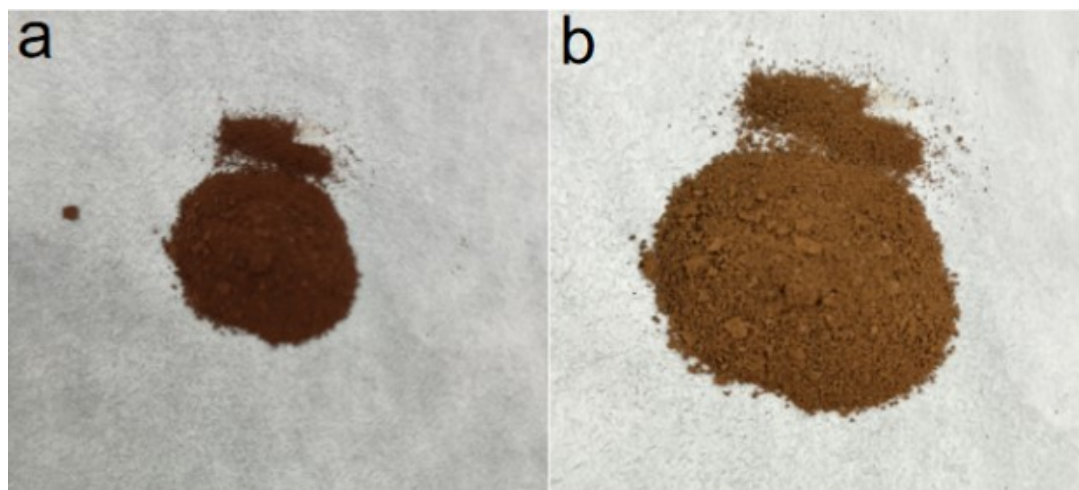


Fig. S2 a) V_0 -FeOOH powder and b) FeOOH powder sample.



Fig. S3 V_2O_5 -FeOOH, FeOOH, and IrO_2 ink-loaded electrodes and Ni foam (From left to right).

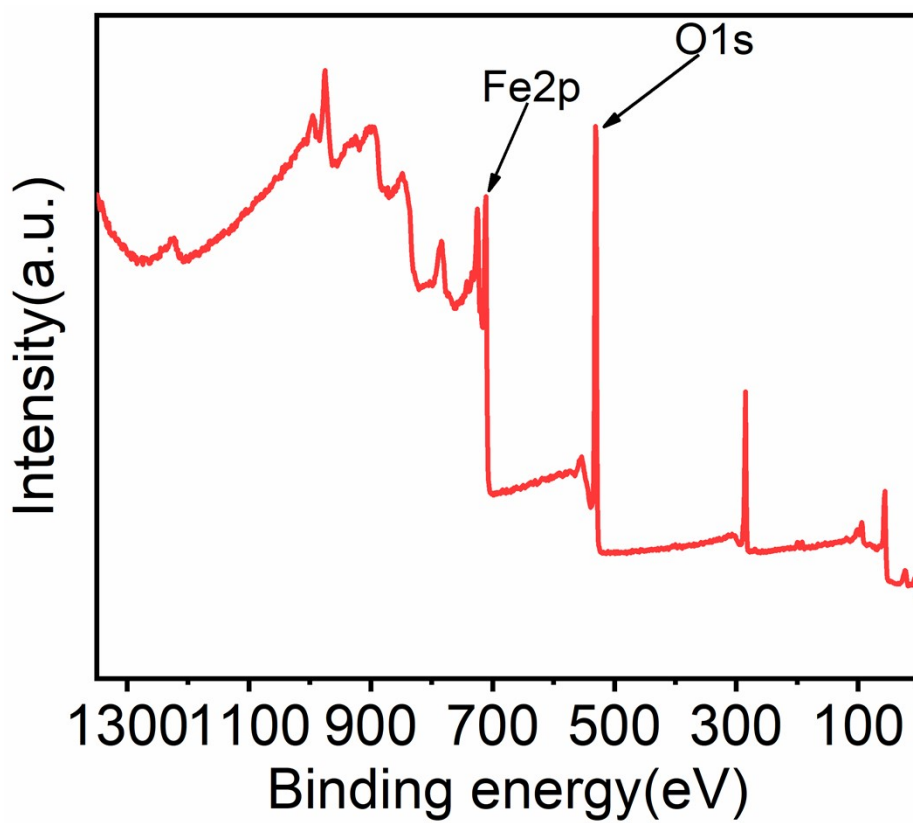


Fig. S4 XPS survey scan of V_0 -FeOOH sample.

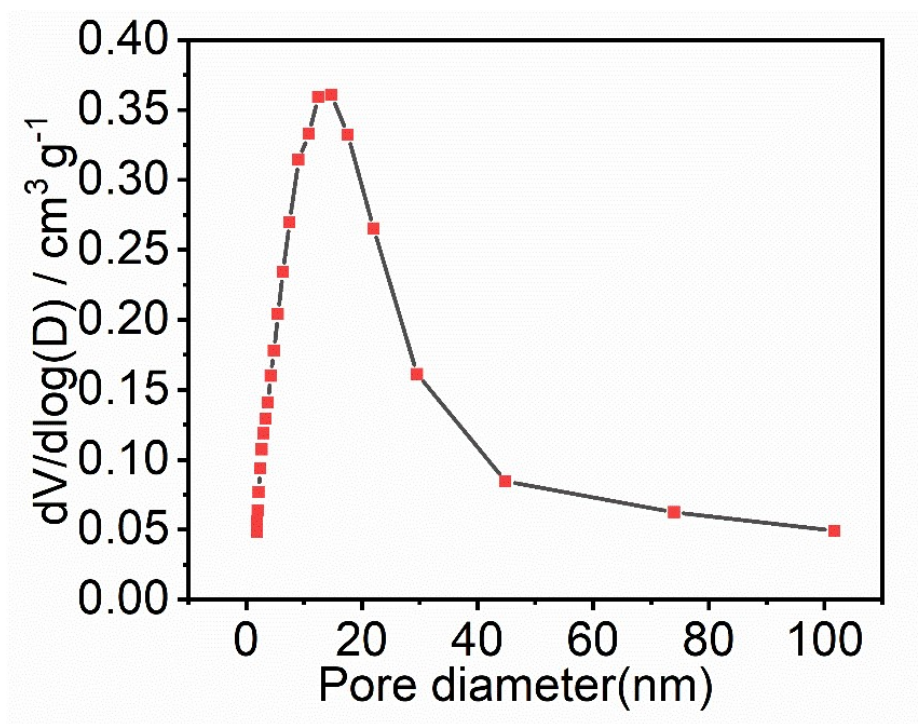


Fig. S5 The Barrett-Joyner-Halenda(BJH) pore size distribution for VO-FeOOH sample.

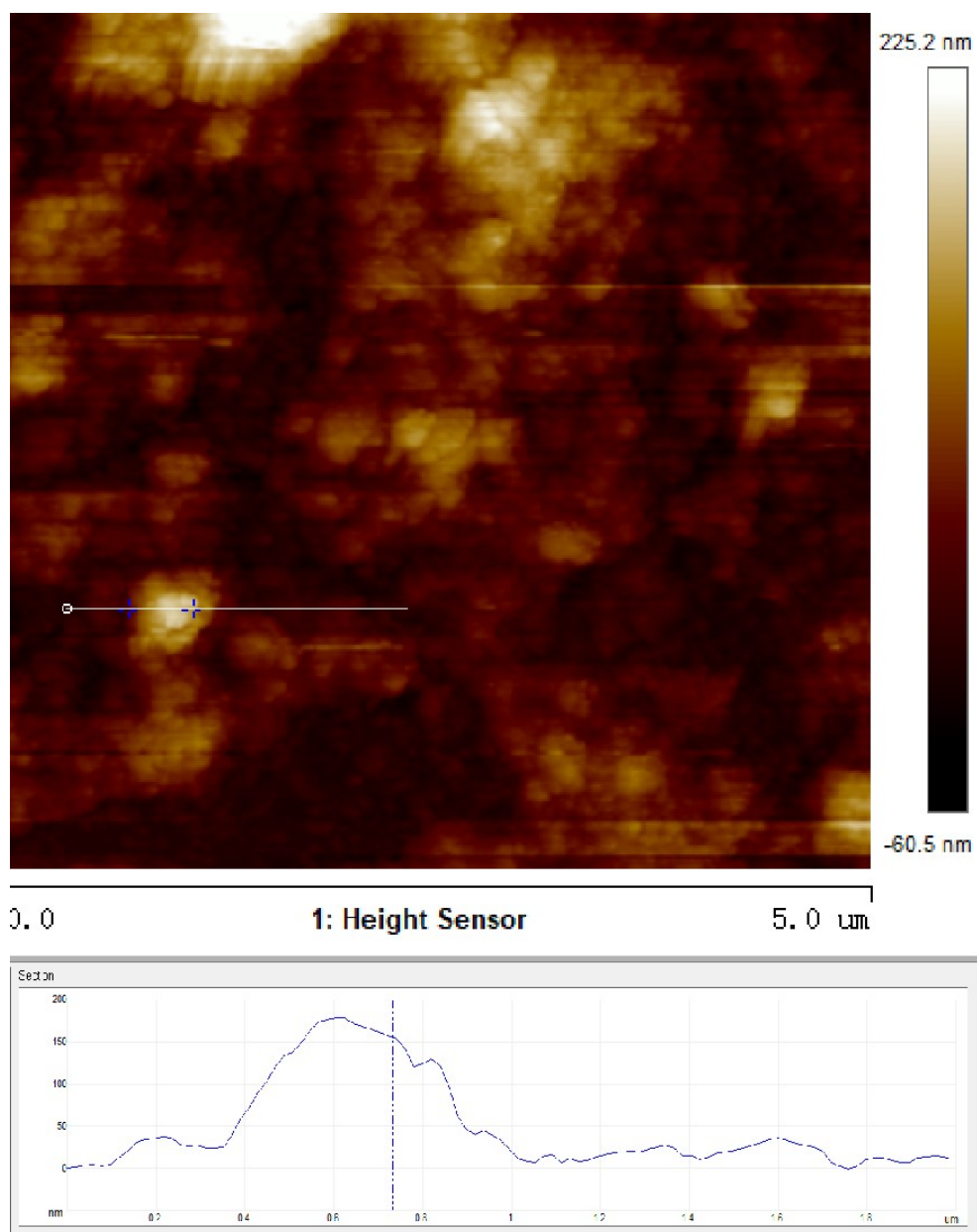


Fig. S6 AFM image of V_O -FeOOH sample.

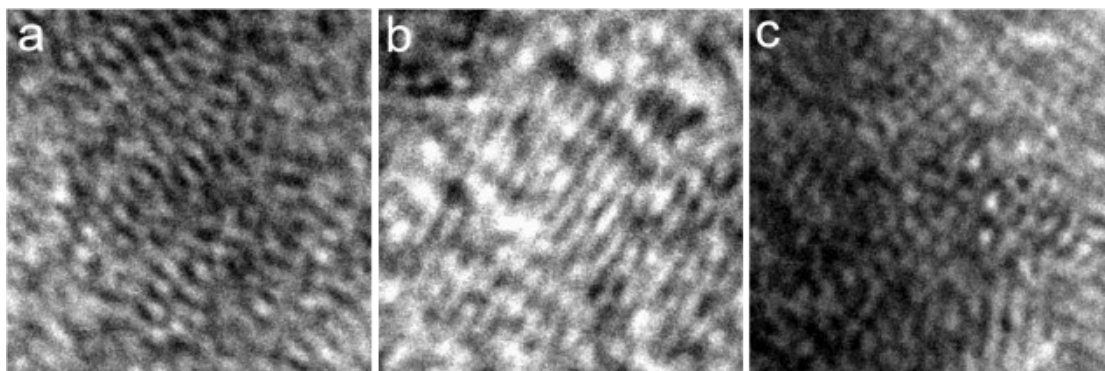


Fig. S7 The inverse fast Fourier transform(FFT) of V_O -FeOOH sample based different regions (a, I) (b, II) (c, III) .

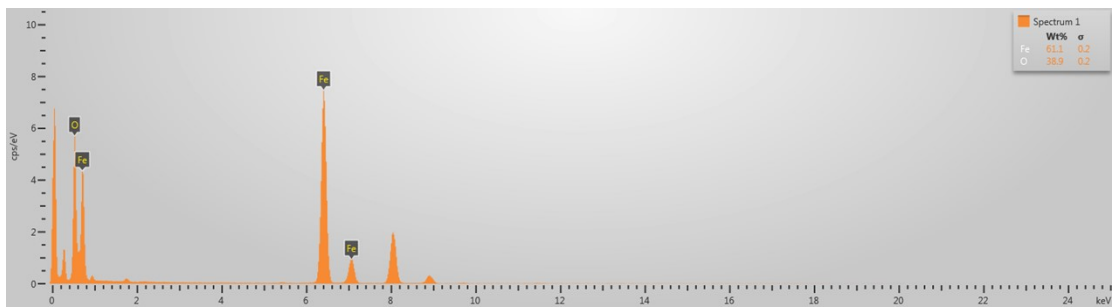


Fig. S8 The EDS of V₀-FeOOH sample.

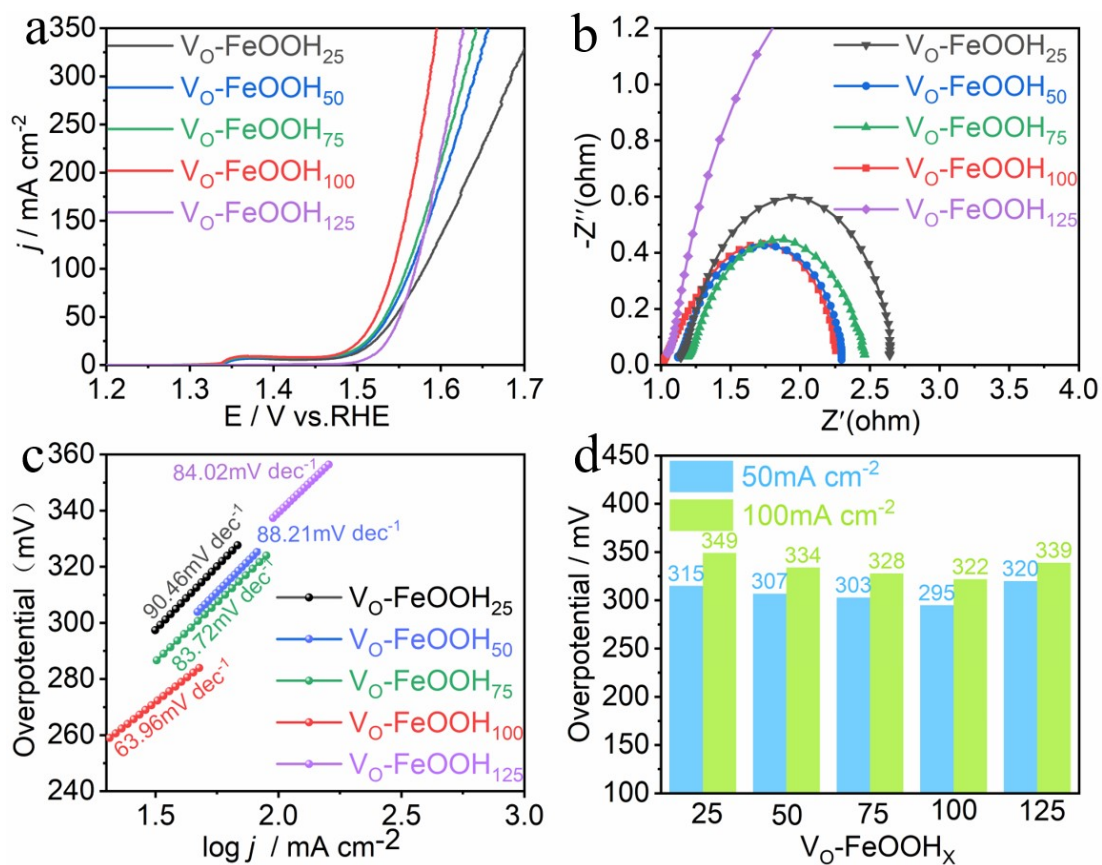


Fig. S9 Electrochemical properties of $\text{V}_\text{O}\text{-FeOOH}$ with different loadings (25, 50, 75, 100, 125 μL). a) LSV curves, b) EIS, c) Tafel slopes, d) overpotentials based 50 and 100 mA cm^{-2} .

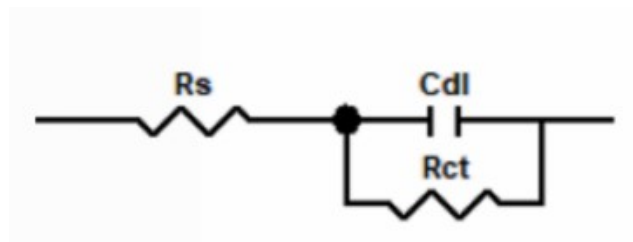


Fig. S10 The electrochemical impedance spectroscopy equivalent circuit diagram.

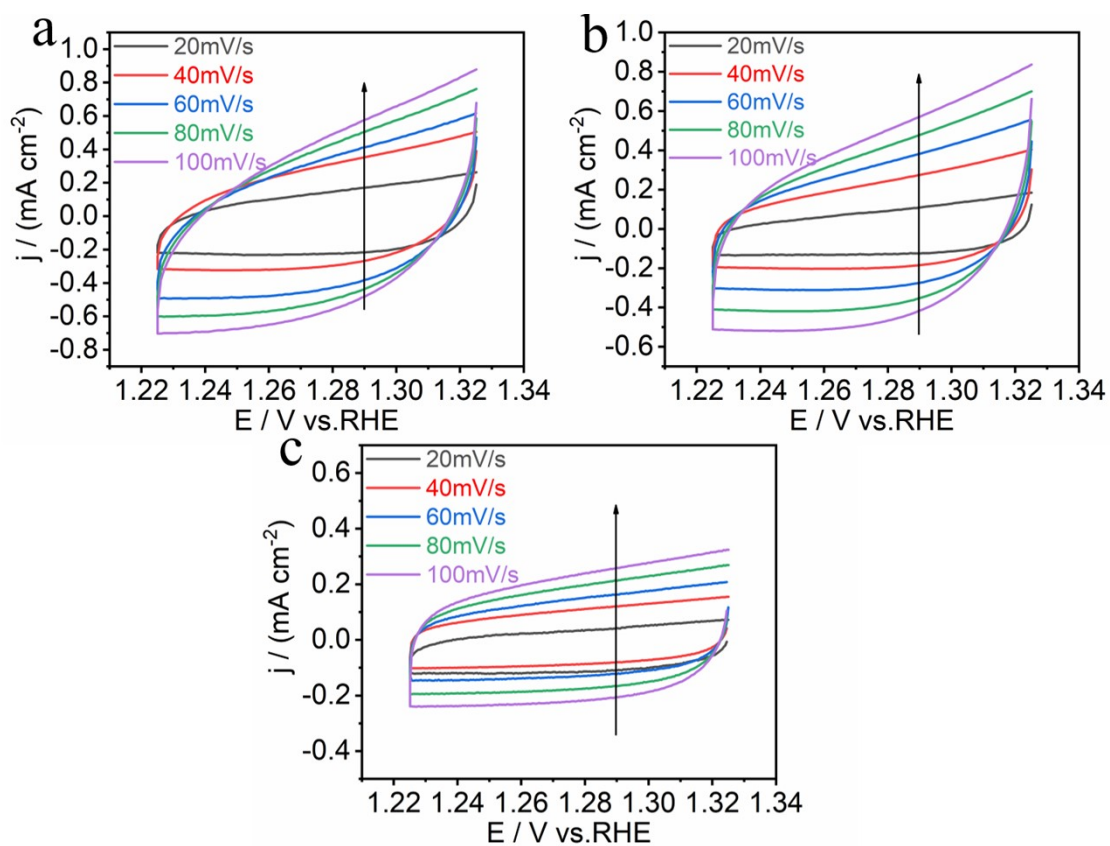


Fig. S11 CV curves of electrodes at different scan rates from 20 to 100 mV s^{-1} . a) V_O -FeOOH, b) IrO_2 , c) NF.

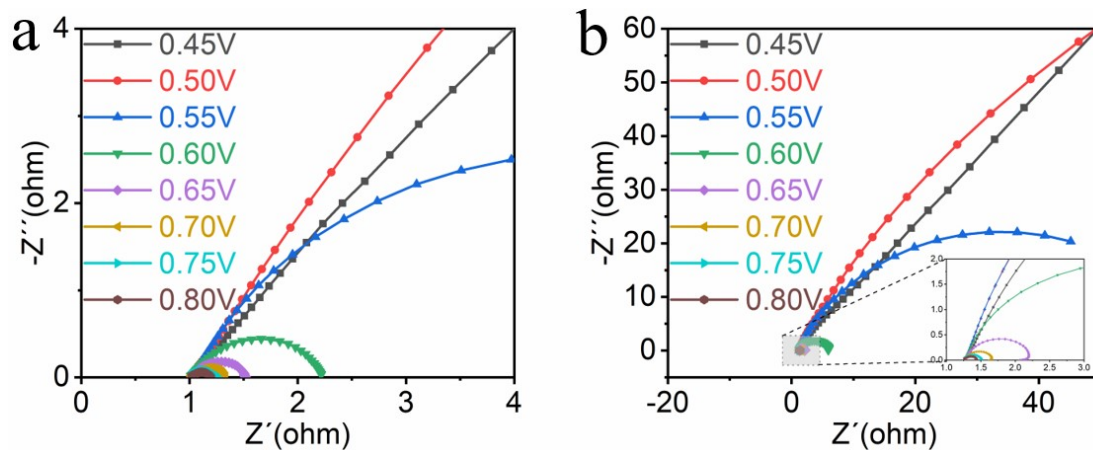


Fig. S12 The Operando Nyquist of a) IrO₂ and b) NF at various overpotentials in 1.0 M KOH electrolyte. (Inset in Fig. S3b: partially enlarged image).

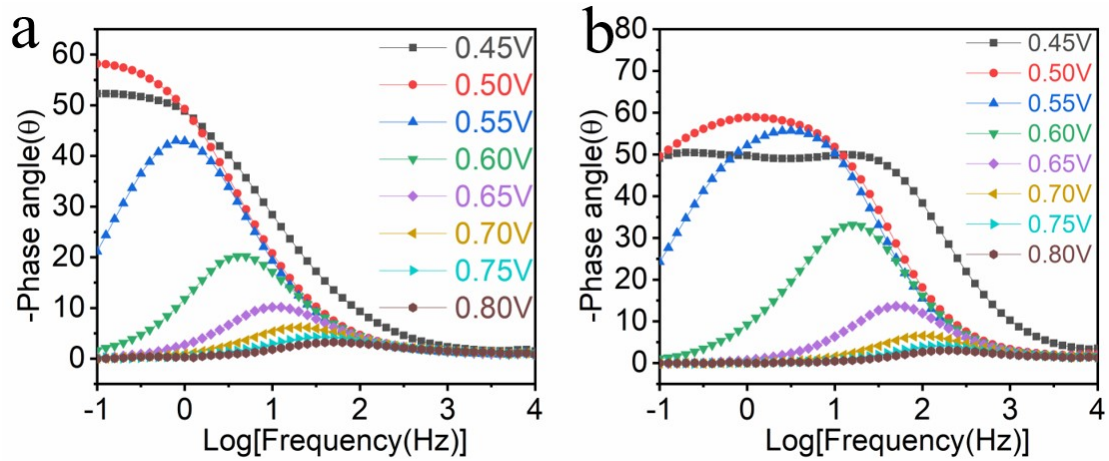


Fig. S13 The Bode phase plots of a) IrO₂ and b) NF at various overpotential in 1.0 M KOH electrolyte.

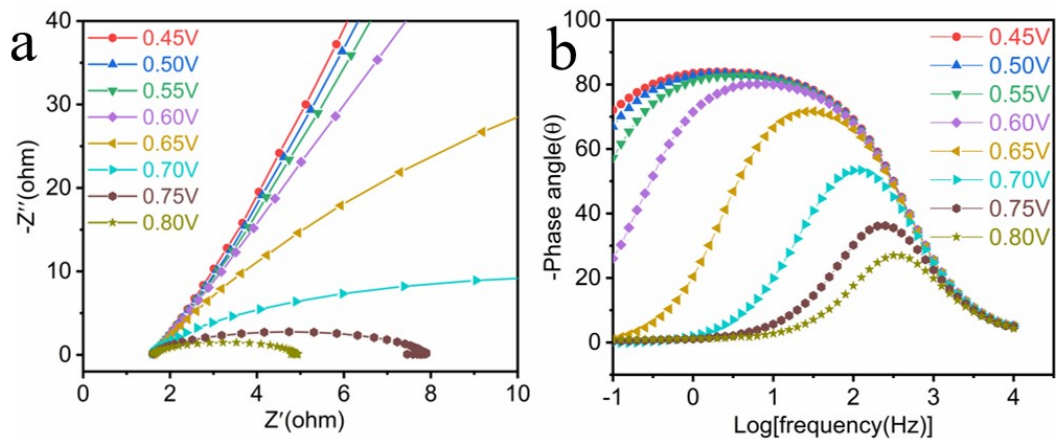


Fig. S14 a) In-situ Nyquist and b) Bode phase diagrams of V_O -FeOOH sample supported on carbon cloth at different overpotentials in 1.0 M KOH electrolyte.

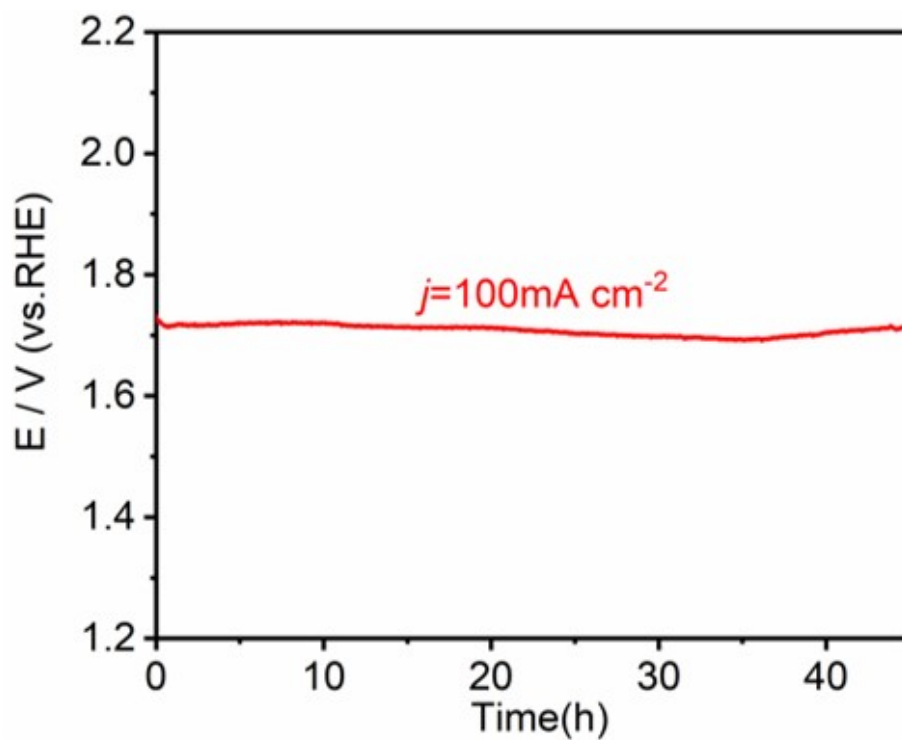


Fig. S15 The long-time E-t curve of V_O -FeOOH for OER under a constant current of 100mA cm^{-2} .

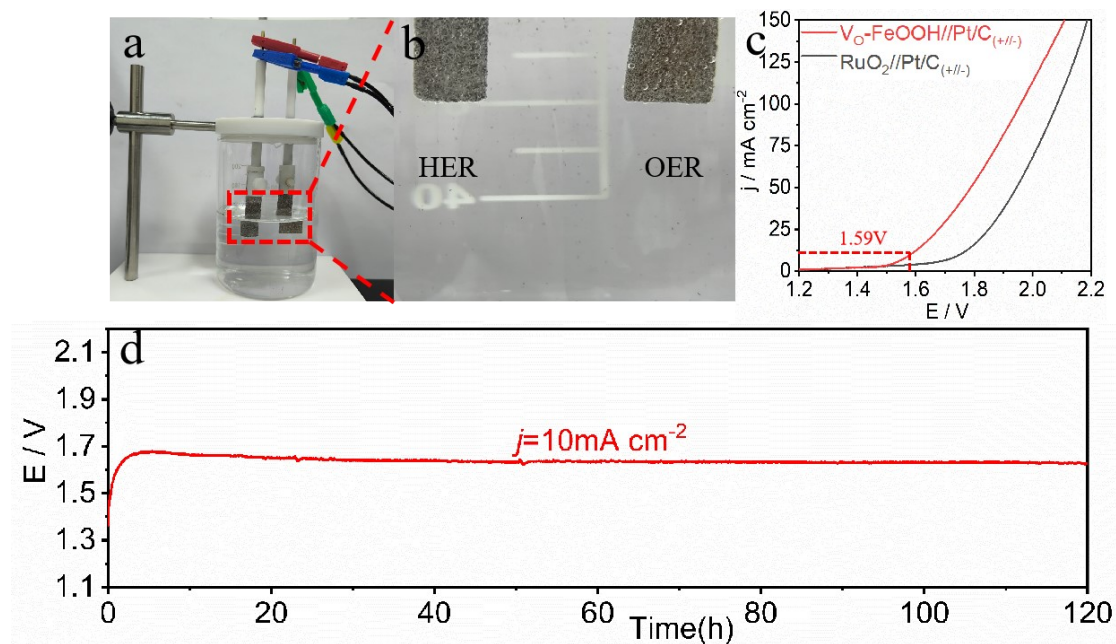


Fig. S16 a) The two-electrode water splitting device diagram, b) amplification schematic diagram of two-electrode water splitting device, c) LSV plots of the $\text{V}_\text{O}\text{-FeOOH//Pt/C}$, $\text{RuO}_2\text{//Pt/C}$ for overall alkaline water splitting, d) E-t curve of $\text{V}_\text{O}\text{-FeOOH//Pt/C}$ for overall water splitting at 10 mA cm^{-2} in 1.0 M KOH electrolyte.

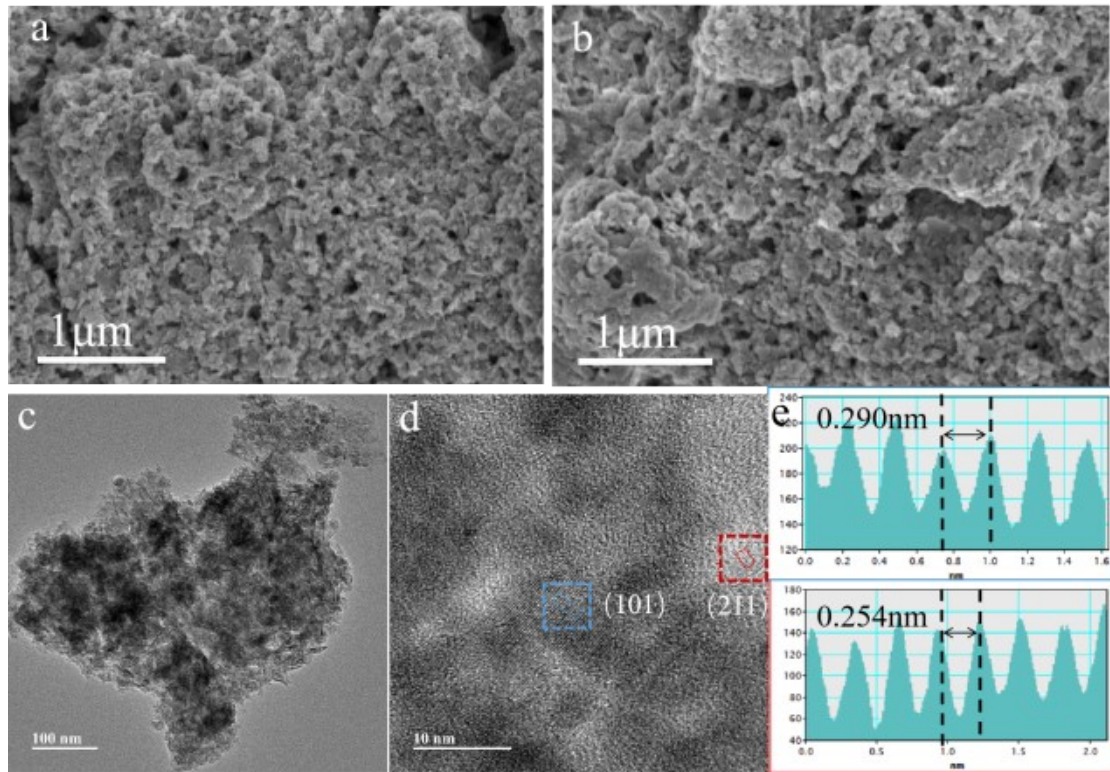


Fig. S17 a) SEM image of V_O -FeOOH before OER and b) SEM image, c) TEM image, d) HRTEM image, e) the different regions corresponding intensity profiles along with the position of V_O -FeOOH after OER.

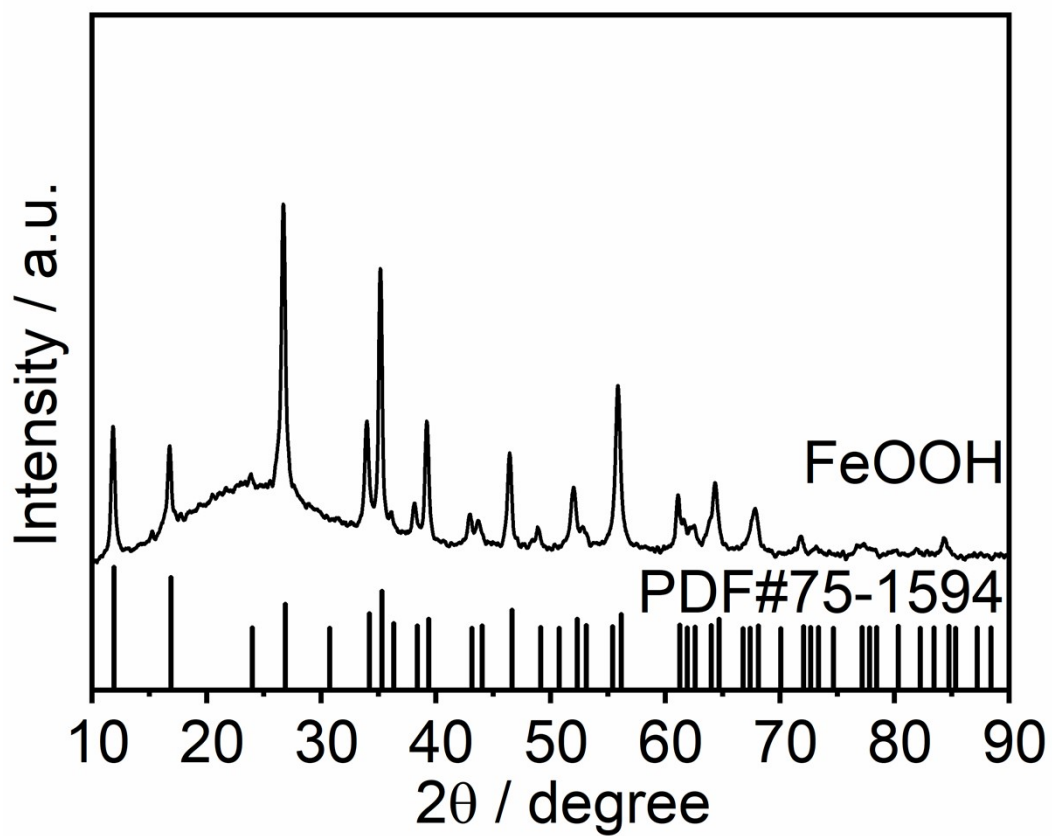


Fig. S18 XRD patterns of FeOOH and standard card.

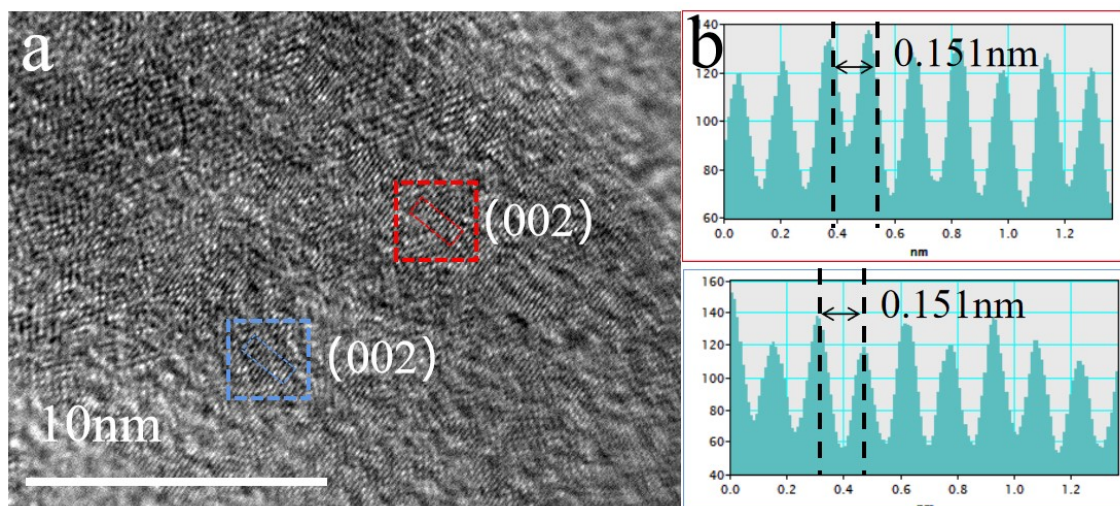


Fig. S19 The a) HRTEM image and b) the different regions corresponding intensity profiles along with the position of FeOOH.

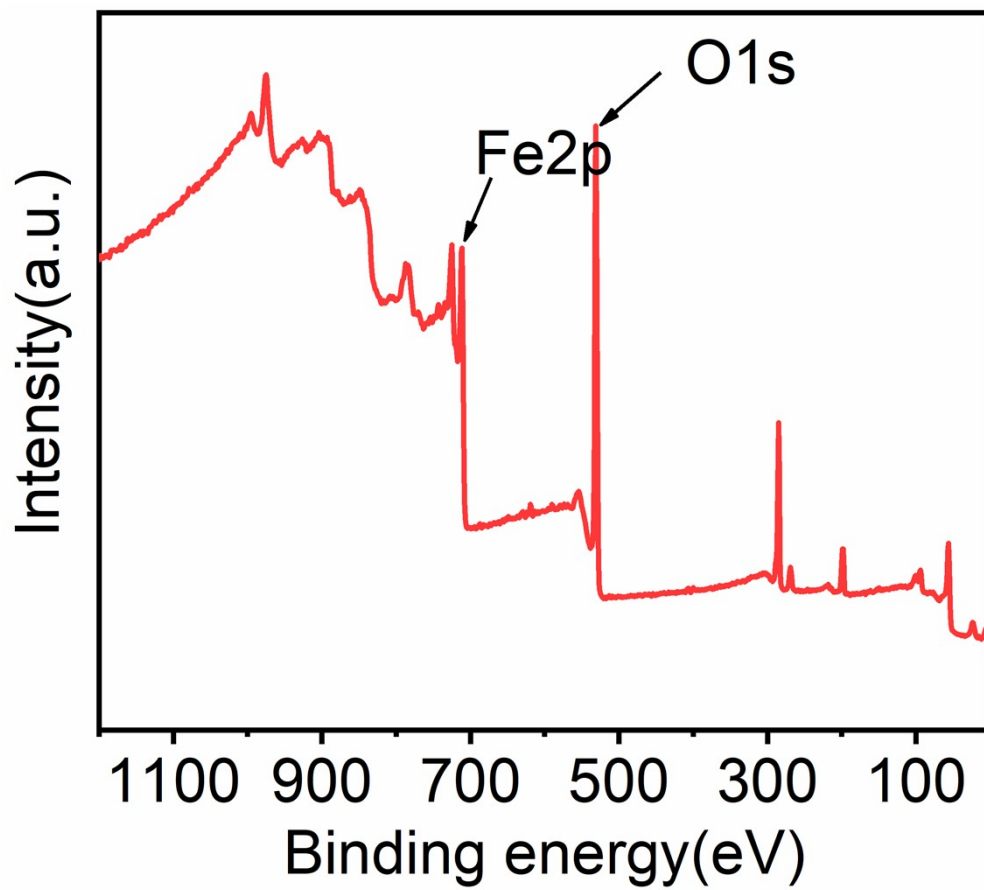


Fig. S20 The XPS spectrum of FeOOH sample.

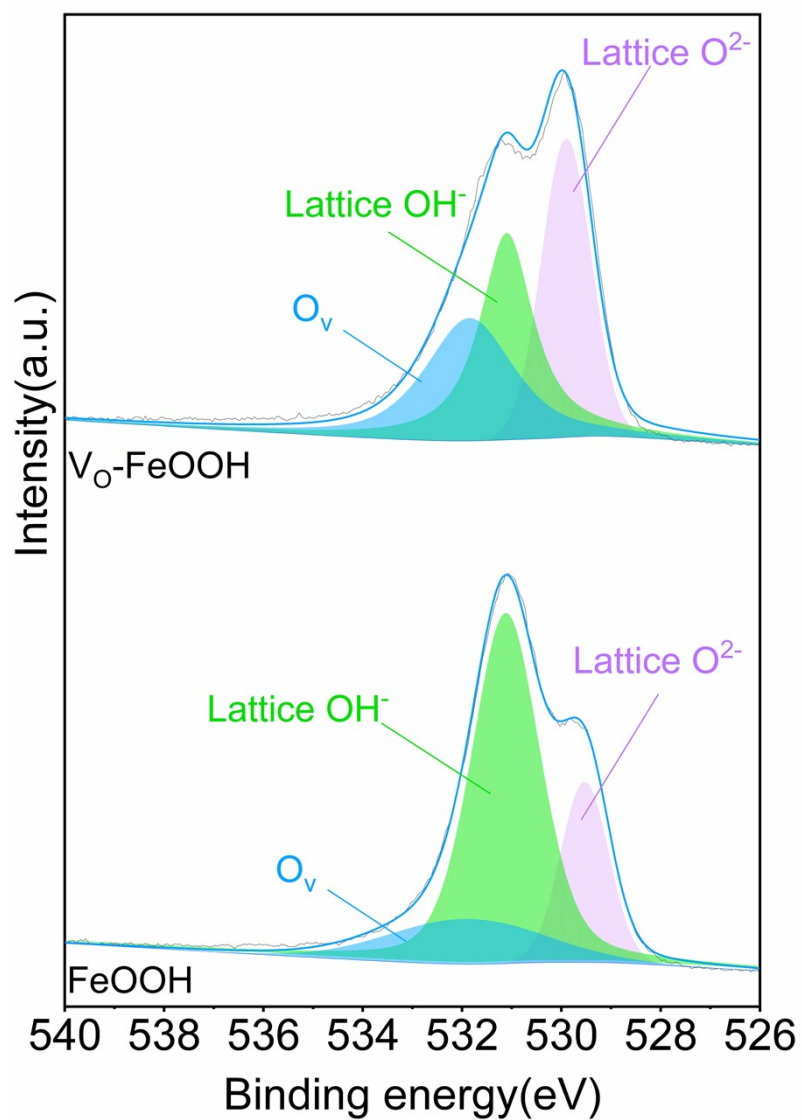


Fig. S21 O1s high resolution XPS spectra of V_O -FeOOH and FeOOH samples.

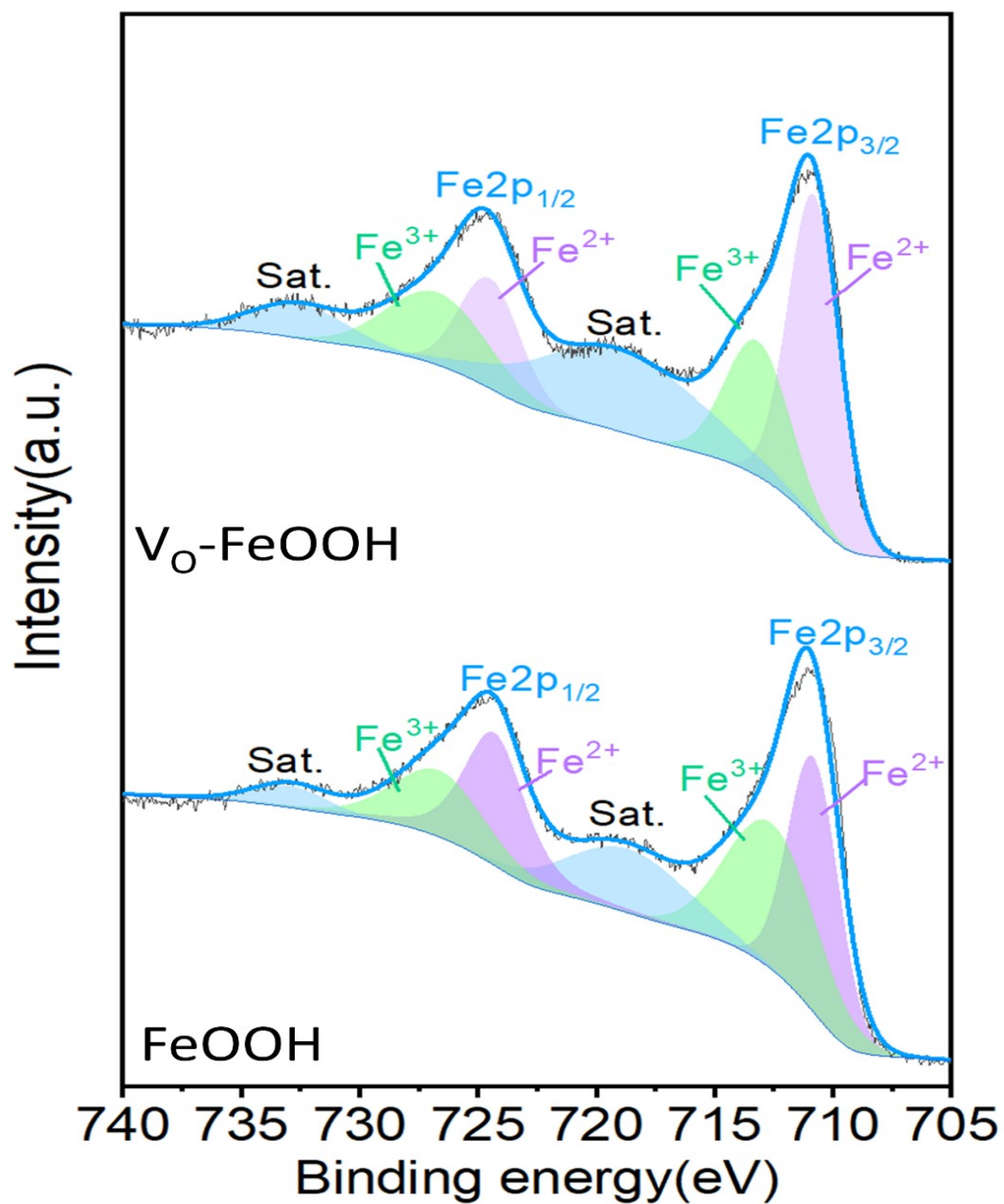


Fig. S22 Fe2p high resolution XPS spectra of $V_O\text{-FeOOH}$ and FeOOH samples.

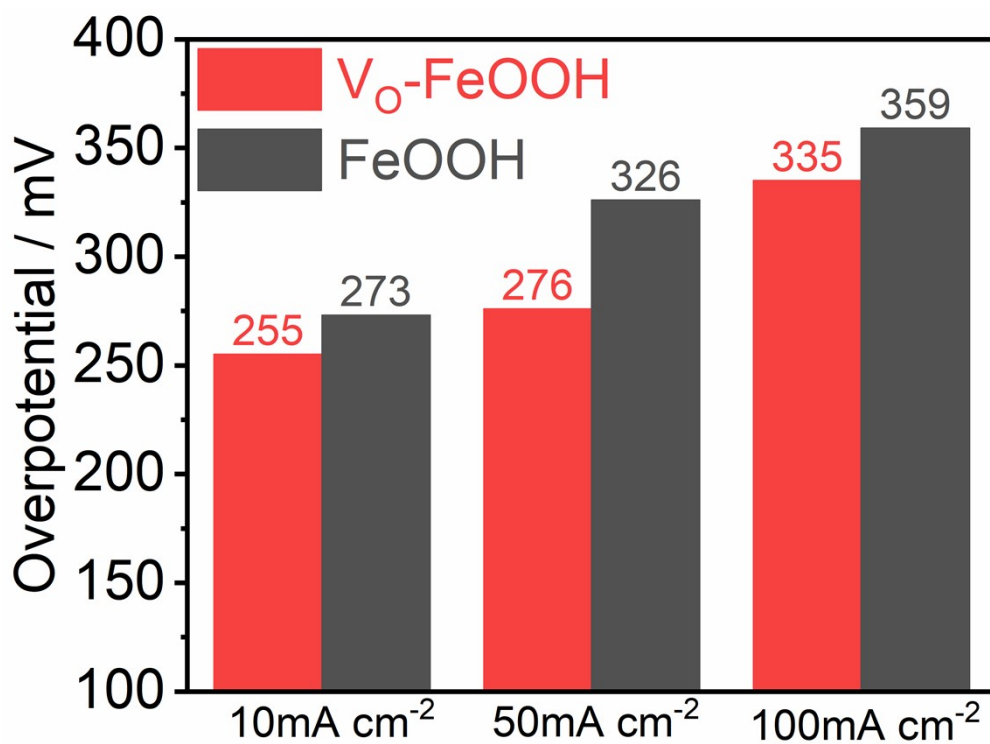


Fig. S23 Comparison of overpotential of V_O-FeOOH and FeOOH samples at different current density.

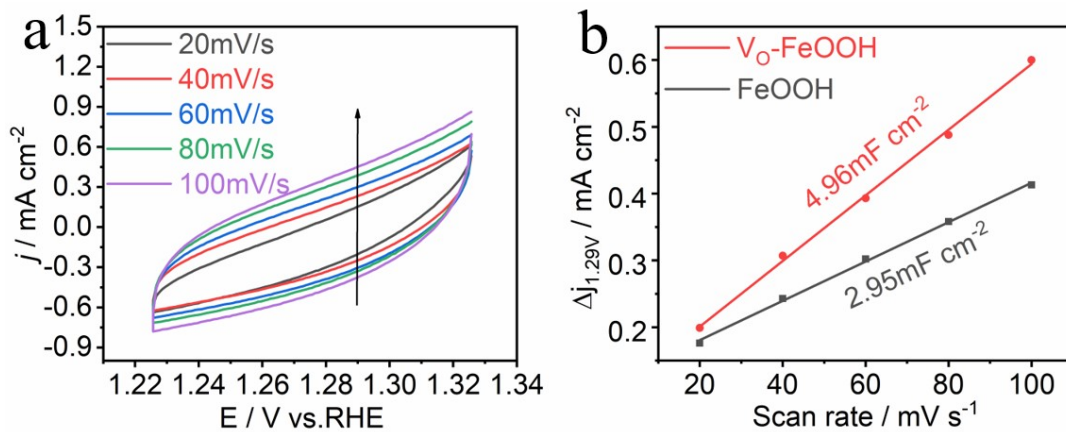


Fig. S24 a) CV curves of electrodes at different scan rates from 20 to 100 mV s^{-1} of FeOOH, b) The C_{dl} obtained at the specific potential of synthesized $V_{\text{O}}\text{-FeOOH}$ and FeOOH samples.

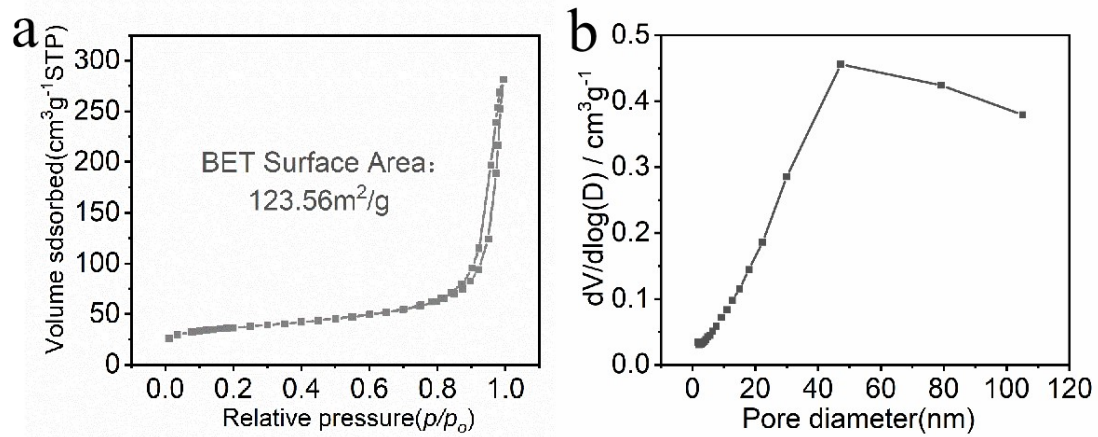


Fig. S25 a) N_2 adsorption-desorption isotherms and b) Barrett-Joyner-Halenda (BJH) pore size distribution for FeOOH sample.

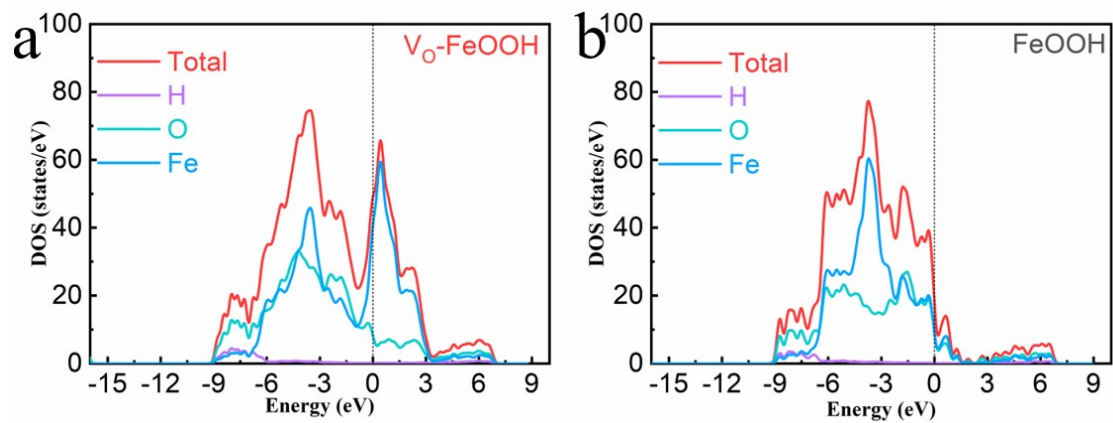


Fig. S26 Density of states of (a) V_O -FeOOH and (b) FeOOH samples, respectively.

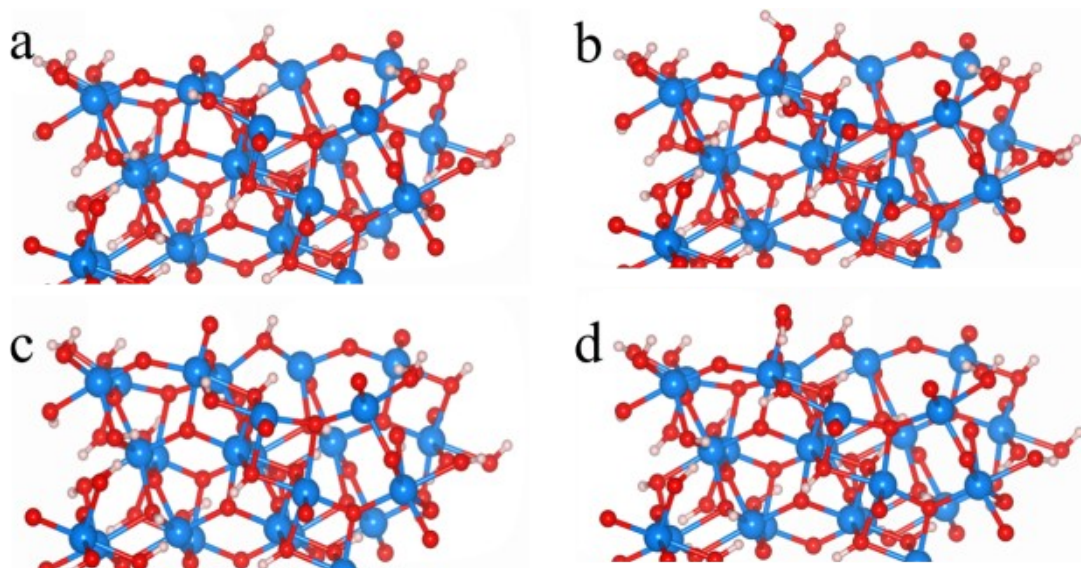


Fig. S27 Optimized configurations of a) V_O-FeOOH and b) O*, c) OH*, and d) OOH* species adsorbed on V_O-FeOOH sample.

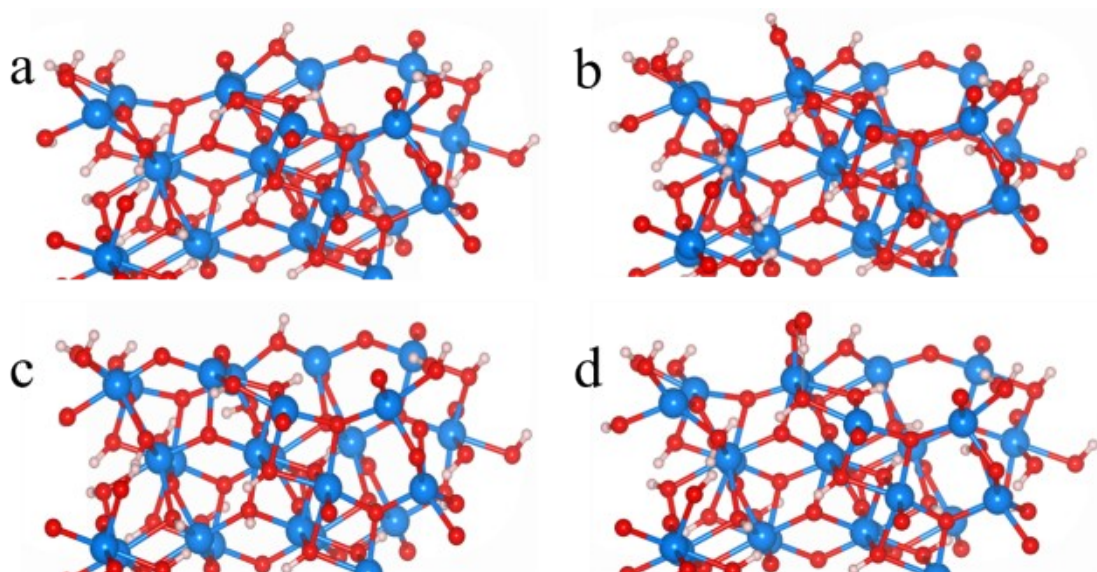


Fig. S28 Optimized configurations of a) FeOOH and b) O*, c) OH*, and d) OOH* species adsorbed on FeOOH samples.

3. Supplementary Tables

Table S1. Comparison of the OER performance of V_O-FeOOH catalyst with other reported OER catalysts

Catalyst	Electrolyte	Current density/mA cm ⁻²	Overpotential / mV	catalyst loading/mg cm ⁻²	Reference
δ-FeOOH	1M KOH	10	265	2.50	11
F(V)OOH-1.5	1M KOH	10	232	1.92	12
α-FeOOH nanorod	1M KOH	10	333	3.00	13
FeOOH SHTs	1M KOH	10	245	4.00	14
CoOOH	1M KOH	10	295	-----	15
S-FeOOH	1M KOH	10	244	0.29	16
NiOOH/Fe ₂ O ₃	1M KOH	10	325	-----	17
CoCuFe-S	1M KOH	10	300	0.23	18
Co-B film	1M KOH	10	280	-----	19
ZnCo ₂ O ₄ /FeOOH	1M KOH	10	299	0.21	20
FeCo@C	1M KOH	10	302	0.08	21
Fe-CoOOH/G	1M KOH	10	330	0.04	22
FeCo-LDH/PANI	1M KOH	10	323	2.00	23
NiCoP/C@FeOOH	1M KOH	10	271	0.26	24
FeOOH@Ni(OH) ₂	1M KOH	10	310	0.25	25
FeOOH/CoO	1M KOH	10	256	4.00	26
FeOOH-LaNiO ₃	1M KOH	10	360	0.23	27
V _O -FeOOH	1M KOH	10	255	0.49	This work

4. Reference

1. J. Lu, Z. Wang, Y. Guo, Z. Jin, G. Cao, J. Qiu, F. Lian, A. Wang, W. Wang, Ultrathin nanosheets of FeOOH with oxygen vacancies as efficient polysulfide electrocatalyst for advanced lithium–sulfur batteries. *Energy Stor. Mater.* **2022**, *47*, 561-568.
2. J.-J. Zhang, W.-W. Bao, X.-H. Feng, C.-M. Yang, N.-L. Wang, Y.-J. Qiu, J.-T. Li, P.-F. Zhang, Z.-H. Luo, Layered double hydroxides as a robust catalyst for water oxidation through strong substrate-catalytic layer interaction. *Int. J. Hydrogen Energy* **2023**.
3. G. Kresse, J. Furthmüller, Efficient iterative schemes for ab initio total-energy calculations using a plane-wave basis set. *Phys. Rev. B* **1996**, *54*, 11169-11186.
4. J. P. Perdew, K. Burke, M. Ernzerhof, Generalized Gradient Approximation Made Simple. *Phys. Rev. Lett.* **1996**, *77*, 3865-3868.
5. Y. Zhang, W. Yang, Comment on "Generalized Gradient Approximation Made Simple". *Phys. Rev. Lett.* **1998**, *80*, 890-890.
6. B. Hammer, L. B. Hansen, J. K. Nørskov, Improved adsorption energetics within density-functional theory using revised Perdew-Burke-Ernzerhof functionals. *Phys. Rev. B* **1999**, *59*, 7413-7421.
7. H. J. Monkhorst, J. D. Pack, Special points for Brillouin-zone integrations. *Phys. Rev. B* **1976**, *13*, 5188-5192.
8. P. E. Blöchl, Projector augmented-wave method. *Phys. Rev. B* **1994**, *50*, 17953-17979.
9. S. Grimme, J. Antony, S. Ehrlich, H. Krieg, A consistent and accurate ab initio parametrization of density functional dispersion correction (DFT-D) for the 94 elements H-Pu. *J. Chem. Phys.* **2010**, *132*.
10. J. Masa, P. Weide, D. Peeters, I. Sinev, W. Xia, Z. Sun, C. Somsen, M. Muhler, W. Schuhmann, Amorphous Cobalt Boride (Co₂B) as a Highly Efficient Nonprecious Catalyst for Electrochemical Water Splitting: Oxygen and Hydrogen Evolution. *Adv. Energy Mater.* **2016**, *6*, 1502313.
11. X. Ji, C. Cheng, Z. Zang, L. Li, X. Li, Y. Cheng, X. Yang, X. Yu, Z. Lu, X. Zhang, H. Liu, Ultrathin and porous δ-FeOOH modified Ni₃S₂ 3D heterostructure nanosheets with excellent alkaline overall water splitting performance. *J. Mater. Chem. A* **2020**, *8*, 21199-21207.
12. F. N. I. Sari, H.-S. Chen, A. k. Anbalagan, Y.-J. Huang, S.-C. Haw, J.-M. Chen, C.-H. Lee, Y.-H. Su, J.-M. Ting, V-doped, divacancy-containing β-FeOOH electrocatalyst for high performance oxygen evolution reaction. *Chem. Eng. J.* **2022**, *438*, 135515.
13. C. Manjunatha, N. Srinivasa, S. Samriddhi, C. Vidya, S. Ashoka, Studies on anion-induced structural transformations of iron(III) (Hydr)oxide micro-nanostructures and their oxygen evolution reaction performance. *Solid State Sciences* **2020**, *106*, 106314.
14. Y. Zhang, X.-A. Teng, Z.-Q. Ma, R.-M. Wang, W.-M. Lau, A.-X. Shan, Synthesis of FeOOH scaly hollow tubes based on Cu₂O wire templates toward high-efficiency oxygen evolution reaction. *Rare Metals* **2023**, *42*, 1836-1846.
15. S. Ye, J. Wang, J. Hu, Z. Chen, L. Zheng, Y. Fu, Y. Lei, X. Ren, C. He, Q. Zhang, J. Liu, Electrochemical Construction of Low-Crystalline CoOOH Nanosheets with Short-Range Ordered Grains to Improve Oxygen Evolution Activity. *ACS Catal.* **2021**, *11*, 6104-6112.
16. X. Chen, Q. Wang, Y. Cheng, H. Xing, J. Li, X. Zhu, L. Ma, Y. Li, D. Liu, S-Doping Triggers Redox Reactivities of Both Iron and Lattice Oxygen in FeOOH for Low-Cost and High-Performance Water Oxidation. *Adv. Funct. Mater.* **2022**, *32*, 2112674.
17. P. Sagar, K. Yogesh, A. Syed, N. Marraiki, A. M. Elgorban, N. S. S. Zaghloul, S. Ashoka, Studies on the effect of crystalline Fe₂O₃ on OER performance of amorphous NiOOH electrodeposited on

stainless steel substrate. *Chem.Papers* **2022**, *76*, 7195-7203.

18. S. Zhang, Y. Sun, F. Liao, Y. Shen, H. Shi, M. Shao, Co₉S₈-CuS-FeS trimetal sulfides for excellent oxygen evolution reaction electrocatalysis. *Electrochim. Acta* **2018**, *283*, 1695-1701.

19. S. Gupta, H. Jadhav, S. Sinha, A. Miotello, M. K. Patel, A. Sarkar, N. Patel, Cobalt-Boride Nanostructured Thin Films with High Performance and Stability for Alkaline Water Oxidation. *ACS Sustain. Chem. Eng.* **2019**, *7*, 16651-16658.

20. Z. Yu, Y. Bai, N. Zhang, W. Yang, J. Ma, Z. Wang, W. Sun, J. Qiao, K. Sun, Metal-organic framework-derived heterostructured ZnCo₂O₄@FeOOH hollow polyhedrons for oxygen evolution reaction. *J. Alloys Compd.* **2020**, *832*, 155067.

21. X.T. Han, C. Yu, S. Zhou, C.T. Zhao, H.W. Huang, J. Yang, Z.B. Liu, J.J. Zhao, J.S. Qiu, Ultrasensitive Iron Triggered Nanosized Fe-CoOOH Integrated with Graphene for Highly Efficient Oxygen Evolution, **2017**, *7*, 1614-6832.

22. Q. Wu, T. L. Li, W. J. Wang, Y. P. Xiao, High-throughput chainmail catalyst FeCo@C nanoparticle for oxygen evolution reaction, *Int J Hydrogen Energy*, 2020, *45*, 26574-26582.

23. X.Q. Han, Z.H. Lin, X.Q. He, L.L. Cui, D.X. Lu, The construction of defective FeCo-LDHs by in-situ polyaniline curved strategy as a desirable bifunctional electrocatalyst for OER and HER, *Int J Hydrogen Energy*, **2020**, *45*, 26989-26999.

24. J.-G. Li, Y. Gu, H. Sun, L. Lv, Z. Li, X. Ao, X. Xue, G. Hong, C. Wang, Engineering the coupling interface of rhombic dodecahedral NiCoP/C@FeOOH nanocages toward enhanced water oxidation. *Nanoscale* **2019**, *11*, 19959-19968.

25. J. Wang, S. Li, R. Lin, G. Tu, J. Wang, Z. Li, MOF-derived hollow β-FeOOH polyhedra anchored with α-Ni(OH)₂ nanosheets as efficient electrocatalysts for oxygen evolution. *Electrochim. Acta* **2019**, *301*, 258-266.

26. C. Qiu, S. He, Y. Wang, Q. Wang, C. Zhao, Interfacial Engineering FeOOH/CoO Nanoneedle Array for Efficient Overall Water Splitting Driven by Solar Energy. *Chem.Eur. J.* **2020**, *26*, 4120-4127.

27. Z. Zhang, B. He, L. Chen, H. Wang, R. Wang, L. Zhao, Y. Gong, Boosting Overall Water Splitting via FeOOH Nanoflake-Decorated PrBa_{0.5}Sr_{0.5}Co₂O_{5+δ} Nanorods. *ACS Appl. Mater. Interfaces* **2018**, *10*, 38032-38041.